

Structural stability and mechanical properties of Ni_xMo_yN ternary nitrides under high pressure: A first-principles study

Tao Wang(王涛), Ming-Hong Wen(温铭洪), Kai-Xuan Wang(王凯璇), Jia-Mei Liu(刘佳美), Wei-Hua Wang(王伟华), Xu-Ying Wang(王旭颖), and Pei-Fang Li(李培芳)

Citation: Chin. Phys. B, 2026, 35 (**3**): 036102. DOI: 10.1088/1674-1056/ae306f
http://cpb.iphy.ac.cn; http://iopscience.iop.org/cpb

What follows is a list of articles you may be interested in

Structural evolution and bandgap modification of a robust mixed-valence compound $Eu_9MgS_2B_{20}O_{41}$ under pressure

Boyang Fu(符博洋), Wenfeng Zhou(周文风), Fuyang Liu(刘扶阳), Luhong Wang(王鲁红), Haozhe Liu(刘浩哲), Sheng-Ping Guo(郭胜平), and Weizhao Cai(蔡伟照)

Chin. Phys. B, 2025, 34 (**8**): 086102. DOI: 10.1088/1674-1056/add4e1

High pressure synthesis, crystal structure and electronic properties of $Ba_3Hf(Se_{1-x}Te_x)5$ (x = 0-1)

Zelong Wang(王泽龙), Guodong Wang(王国东), Wenmin Li(李文敏), Runteng Chen(陈润滕), Lei Duan(段磊), Jianfa Zhao(赵建发), Zheng Deng(邓正), Jianfeng Zhang(张建丰), Tingjiang Yan(颜廷江), Jun Zhang(张俊), Xiancheng Wang(望贤成), and Changqing Jin(靳常青)

Chin. Phys. B, 2025, 34 (**8**): 086101. DOI: 10.1088/1674-1056/adcea2

Layer-dependent structural stability and electronic properties of $CrPS_4$ under high pressure

Jian Zhu(朱健), Dengman Feng(冯登满), Liangyu Wang(王亮予), Liang Li(李亮), Fangfei Li(李芳菲), Qiang Zhou(周强), and Yalan Yan(闫雅兰)

Chin. Phys. B, 2025, 34 (**6**): 066102. DOI: 10.1088/1674-1056/adc65f

General-purpose moment tensor potential for Ga-In liquid alloys towards large-scale molecular dynamics with *ab initio* accuracy

Kai-Jie Zhao(赵凯杰) and Zhi-Gong Song(宋智功)

Chin. Phys. B, 2025, 34 (**6**): 066101. DOI: 10.1088/1674-1056/adc661

First-principles insights into the high-pressure stability and electronic characteristics of molybdenum nitride

Tao Wang(王涛), Ming-Hong Wen(温铭洪), Xin-Xin Zhang(张新欣), Wei-Hua Wang(王伟华), Jia-Mei Liu(刘佳美), Xu-Ying Wang(王旭颖), and Pei-Fang Li(李培芳)

Chin. Phys. B, 2025, 34 (**3**): 036104. DOI: 10.1088/1674-1056/adab66

SPECIAL TOPIC — Structures and properties of materials under high pressure

Structural stability and mechanical properties of Ni_xMo_yN ternary nitrides under high pressure: A first-principles study

Tao Wang(王涛), Ming-Hong Wen(温铭洪), Kai-Xuan Wang(王凯璇), Jia-Mei Liu(刘佳美), Wei-Hua Wang(王伟华), Xu-Ying Wang(王旭颖), and Pei-Fang Li(李培芳)†

Extreme Conditions Physics Research Team, College of Physics and Electronic Information, Inner Mongolia Minzu University, Tongliao 028043, *China*

(Received 23 November 2025; revised manuscript received 16 December 2025; accepted manuscript online 23 December 2025)

Transition metal nitrides have attracted significant attention due to their outstanding properties; however, studies on ternary systems under high pressure remain limited. In this work, we systematically investigated the structures and properties of NiMoN compounds in the pressure range of 0–100 GPa by combining crystal structure analysis by particle swarm optimization (CALYPSO) structure prediction with first-principles calculations. To explore more structural possibilities, a large number of candidate structures were predicted and those with potential stability were selected. Among the newly predicted structures, a stable phase $P2_13$-$NiMo_4N$ and a low-energy metastable phase $I4_132$-$NiMo_3N$ are proposed for the first time. The metastable structure $I4_132$-$NiMo_3N$ lies 0.007 eV/atom above the convex hull, whereas the energy of the experimentally synthesized structure $Fd3m$-Ni_3Mo_3N is 0.036 eV/atom above the convex hull. Therefore, $I4_132$-$NiMo_3N$ can likely be obtained through experimental synthesis. Phonon and elastic constant calculations confirm the stability of $P2_13$-$NiMo_4N$ and $I4_132$-$NiMo_3N$, while electronic structure calculations indicate that both exhibit metallic behavior, with Mo-4d orbitals making the primary contribution at the Fermi level. Mechanical property evaluations reveal that $P2_13$-$NiMo_4N$ exhibits high hardness, whereas $I4_132$-$NiMo_3N$ shows relatively lower hardness but enhanced ductility. Under different pressures, both structures exhibit comparable ideal tensile strengths, but their failure mechanisms differ. This study broadens the known structural diversity of NiMoN ternary nitrides and provides theoretical insights into the exploration of high-pressure ternary nitrides.

Keywords: ternary nitride, crystal structure, CALYPSO, high pressure

PACS: 61.50.Ks, 62.20.de, 71.20.–b

DOI: 10.1088/1674-1056/ae306f **CSTR:** 32038.14.CPB.ae306f

1. Introduction

Extreme service environments, such as high temperature, high pressure, and severe wear, place stringent demands on material performance. Traditional hard materials, including diamond and cubic boron nitride (c-BN), exhibit exceptionally high hardness; however, their widespread application is limited by high cost, complex fabrication processes, and inadequate chemical stability. Therefore, the development of novel hard materials has always been a focal point in materials science research. Nitrides, owing to their excellent mechanical properties and chemical stability, occupy an important position in the research of hard materials. For example, TiN,[1–3] CrN,[4–6] and MoN[7–10] have been widely used in protective coatings and cutting tools, whereas ceramic materials such as Si_3N_4[11–13] and AlN[14–16] demonstrate excellent performance in high-temperature applications owing to their thermal resistance and chemical inertness. In addition, nitrides exhibit properties such as high electrical conductivity and catalytic activity. For instance, γ-Mo_2N[17–19] and VN[20–22] have been shown to be excellent catalysts and have been extensively studied for energy conversion processes, including electrocatalytic water splitting. Although nitride materials hold broad application potential in the field of functional materials, current research has largely focused on binary nitride systems, particularly on the crystal structures, mechanical properties, and catalytic performance of binary transition metal nitrides such as TiN, MoN, and CrN.[1–10] As a result, the chemical space of nitride material systems remains far from fully explored. Ternary nitrides, owing to their diverse chemical configurations, bonding modes, and more complex electronic structures, exhibit greater complexity and tunability; however, the number of ternary nitrides that have been successfully synthesized and systematically studied remains relatively limited. The scarcity of ternary nitrides is primarily attributed to the high stability of molecular nitrogen (N_2), which hardly reacts with metals under ambient pressure and requires elevated temperatures to break the N–N triple bond. In addition, nitrides themselves exhibit high cohesive energy and low atomic diffusion rates, while the entropic effect at high temperatures is unfavorable for the incorporation of nitrogen atoms into the solid phase. These factors collectively render the experimental synthesis of ternary nitrides challenging.

In ternary nitride systems, NiMoN compounds can adopt densely packed structures, in which the relatively large atomic

†Corresponding author. E-mail: lipeifang82@163.com

© 2026 Chinese Physical Society and IOP Publishing Ltd. All rights, including for text and data mining, AI training, and similar technologies, are reserved.

radius of Mo and the strong involvement of d orbitals facilitate the formation of crystal structures with locally diverse coordination environments around Ni and N atoms. Such high bond-energy structures render these compounds particularly stable under high pressure, exhibiting low compressibility and high elastic moduli and hardness. Previous studies on ternary Ni_xMo_yN compounds have primarily focused on three structures: Ni_2Mo_3N,[23–28] Ni_3Mo_3N[29–31] and Ni_2Mo_4N.[31] Among these, Ni_2Mo_3N has been the most extensively studied and can be synthesized experimentally via methods such as high-temperature ammonolysis and reduction-nitridation reactions. Herle *et al.*[23] and Weil *et al.*[32] experimentally proposed that Ni_2Mo_3N crystallizes in a cubic β-Mn-type structure (space group $P4_132$) with a lattice parameter of 6.634 Å. Errandonea *et al.*[33] reported that Ni_2Mo_3N exhibits a Vickers hardness of 20.5 GPa, a bulk modulus of 317.4 GPa, and a Young's modulus of 392 GPa, and demonstrates strong compressive resistance and stability under high pressure up to 50 GPa. In addition, Ni_2Mo_3N exhibits remarkable catalytic activity for ammonia decomposition. Zaman *et al.*[34] demonstrated that Ni_2Mo_3N is a promising material, achieving an ammonia conversion rate exceeding 90% at 600 °C. Hund *et al.*[24] also investigated the high-temperature behavior of Ni_2Mo_3N in flowing ammonia at 875 °C. Another ternary nitride, Ni_3Mo_3N, is considered a highly efficient catalyst. Bem *et al.*[35] first reported that Ni_3Mo_3N adopts a cubic η-carbide-type structure with lattice parameters $a = 6.635$ Å, $b = 6.668$ Å, and $c = 6.573$ Å, belonging to the space group $Fd3m$. Recently, Tang *et al.*[29] designed and synthesized a novel ternary nitride heterostructure catalyst, Co_3Mo_3N/Ni_3Mo_3N, which exhibits excellent electrocatalytic performance; Ni_3Mo_3N was synthesized via a nitridation reaction of the $NiMoO_4 \cdot xH_2O$ precursor. In addition to the extensively studied Ni_2Mo_3N and Ni_3Mo_3N, Chen *et al.*[31] performed a theoretical investigation of Ni_2Mo_4N using first-principles methods. Ni_2Mo_4N also adopts a cubic η-type structure with space group $Fd3m$ and a lattice parameter of $a = 11.374$ Å. A comparison of the energies of Ni_3Mo_3N and Ni_2Mo_4N further indicates that Mo atoms can effectively reduce the compound energy in ternary nitrides, thereby stabilizing the nitride.

High pressure, as an important means of tuning material structures and properties, can significantly modify the crystal structures and bonding patterns of materials, thereby inducing phase transitions, enhancing mechanical properties, and generating new phases and structures that are unstable under ambient pressure. However, research on ternary nitrides under high pressure remains scarce. In the Ni–Mo–N system, most studies have concentrated on synthesis strategies and catalytic performance under ambient conditions, whereas structural investigations at high pressure are still limited, and comprehensive theoretical studies on the possible high-pressure phases and their properties are lacking. Therefore, applying crystal structure prediction methods to systematically investigate the NiMoN ternary nitride system under high pressure offers an effective approach to elucidate its structural evolution, identify potentially stable phases, and expand the structural landscape of ternary nitrides.

In this research, the crystal structure analysis by particle swarm optimization (CALYPSO) code[36–42] was employed to predict the structures of the Ni–Mo–N ternary nitrides under varying pressures based on energy minimization. Details of the CALYPSO algorithm and its applications can be found in Refs. [43–45]. We primarily used the CALYPSO software to predict the structures of $P2_13$-$NiMo_4N$ and $I4_132$-$NiMo_3N$ and validated their stability. We calculated both their electronic and mechanical properties, with a focus on analyzing the shear and tensile stress–strain behavior of these structures under varying pressure conditions.

2. Calculational method

Structural predictions for the Ni_xMo_yN ternary nitrides were made using CALYPSO within the pressure range of 0–100 GPa, and the accuracy of CALYPSO has been well validated in previous studies.[46–52] Density functional theory (DFT) calculations[53,54] were carried out using the Vienna *ab initio* simulation package (VASP)[55] with the exchange–correlation functional represented by the Perdew–Burke–Ernzerhof (PBE) form within the generalized gradient approximation (GGA).[56] The $3p^63d^84s^2$, $4p^64d^55s^1$, and $2s^22p^3$ electrons were treated as valence electrons for Ni, Mo, and N atoms, respectively. The projector-augmented wave (PAW) method was applied, utilizing PAW potentials from the VASP library. A cutoff energy of 560 eV was used. To ensure enthalpy convergence within 1 meV/atom, Monkhorst–Pack (MP) grids of $7 \times 7 \times 7$ for $P2_13$-$NiMo_4N$ and $6 \times 6 \times 6$ for $I4_132$-$NiMo_3N$ were employed. Additionally, the differential charge density and phonon dispersion curves were calculated using the Device Studio-projector augmented wave (DS-PAW) software integrated within the device studio program.[57] The phonon spectrum was calculated using the supercell method based on finite displacements.[58] For both $P2_13$-$NiMo_4N$ and $I4_132$-$NiMo_3N$, a $2 \times 2 \times 2$ supercell was employed.

3. Results and discussion

Ni_xMo_yN structures with different stoichiometries were explored at 0 GPa, 50 GPa, and 100 GPa using the CALYPSO software. Thermodynamically stable Ni_xMo_yN structures were identified by calculating the convex hull energies of compounds with various compositions, and the corresponding convex hull diagrams were constructed. The convex hull

energy was calculated using the following expression:

$$E_{\text{hull}}(\text{Ni}_x\text{Mo}_y\text{N}) = E_{\text{form}}^{(\text{a})} - E_{\text{form}}^{(\text{b})}, \tag{1}$$

$$E_{\text{form}} = \frac{E_{\text{total}} - xE(\text{Ni}) - yE(\text{Mo}) - zE(\text{N})}{x+y+z}, \tag{2}$$

where $E_{\text{form}}^{(\text{a})}$ represents the formation energy of the predicted structure, while $E_{\text{form}}^{(\text{b})}$ denotes the lowest formation energy obtained by linear interpolation between other known stable structures on the convex hull. In the ternary convex hull diagram shown in Fig. 1, circles indicate thermodynamically stable structures, whereas diamonds represent metastable structures.

For the stable structures, the predicted Ni_2Mo_3N at ambient pressure agrees well with the experimental results of Herle *et al.*[23] and Weil *et al.*[32] exhibiting a space group of $P4_132$. This structure remains stable under a high pressure of 100 GPa. Moreover, a new cubic phase, $NiMo_4N$ with the $P2_13$ space group, was identified at ambient pressure, along with other metastable structures, including *Fd*3*m*-Ni_3Mo_3N, *Fd*3*m*-Ni_2Mo_4N, $I4_132$-$NiMo_3N$, *P*6*m*2-$NiMo_2N$, and *Cmmm*-NiMoN. At 50 GPa, the stable and metastable structures remain the same as at ambient pressure. Under a high pressure of 100 GPa, additional metastable structures, including *I*4/mmm-Ni_3Mo_4N and *Cmc*2_1-Ni_4Mo_4N, were also identified.

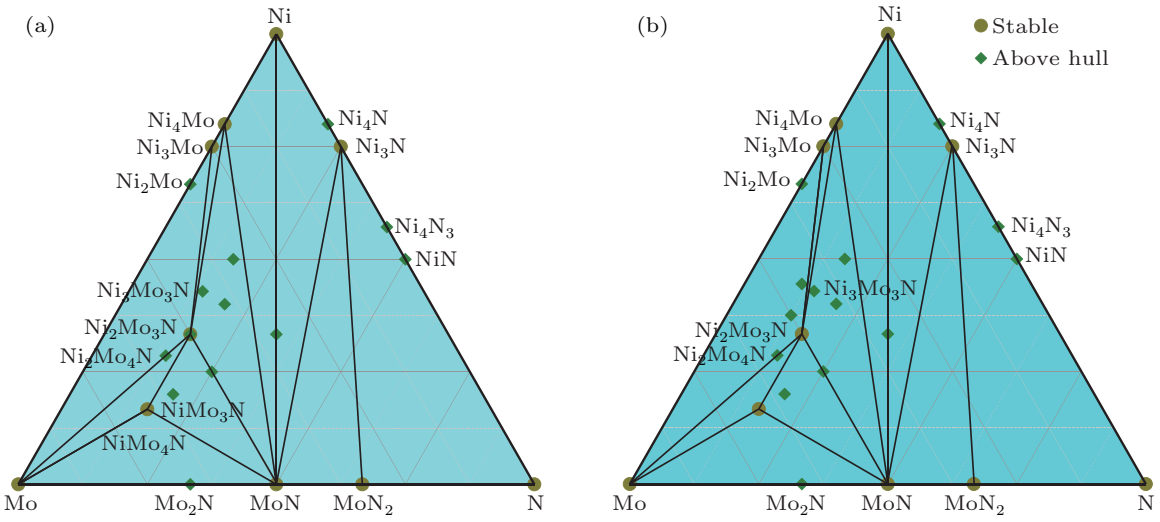


Fig. 1. Convex hull diagrams of Ni_xMo_yN at 0 GPa (a) and 100 GPa (b).

Among the predicted metastable structures at ambient pressure, the cubic $I4_132$-$NiMo_3N$ is only 0.007 eV/atom above the convex hull, while *Fd*3*m*-Ni_3Mo_3N, *Fd*3*m*-Ni_2Mo_4N, and *P*6*m*2-$NiMo_2N$ are 0.036 eV/atom, 0.026 eV/atom, and 0.069 eV/atom above the convex hull, respectively. In contrast, the energies of the other metastable structures are more than 0.1 eV/atom higher than the convex hull. According to the Inorganic Crystal Structure Database, approximately 20% of experimentally synthesized materials are metastable, with some even exhibiting positive formation enthalpies exceeding 0.04 eV/atom.[59,60] Among the structures predicted above, *Fd*3*m*-Ni_3Mo_3N and *Fd*3*m*-Ni_2Mo_4N are known structures, and the prediction is consistent with previous studies. *Fd*3*m*-Ni_3Mo_3N has been successfully synthesized experimentally by Bem *et al.*[35] Since the energy of $I4_132$-$NiMo_3N$ is lower than that of the experimentally synthesized *Fd*3*m*-Ni_3Mo_3N, $I4_132$-$NiMo_3N$ can likely be obtained through experimental synthesis. The following discussion focuses on the stable structure $P2_13$-$NiMo_4N$ and the low-energy metastable structure $I4_132$-$NiMo_3N$, both of which have potential for experimental synthesis.

Table 1. $P2_13$-$NiMo_4N$ and $I4_132$-$NiMo_3N$ lattice parameters and atomic Wyckoff positions at 0 GPa.

Structures	Lattice parameters (Å)	Atoms	Wyckoff positions (fractional)			
				x	*y*	*z*
$P2_13$	$a = 6.795$	Ni	4*a*	0.938	0.938	0.938
($NiMo_4N$)	$b = 6.795$	Mo1	12*b*	0.043	0.063	0.204
	$c = 6.795$	Mo2	4*a*	0.327	0.327	0.327
		N	4*a*	0.626	0.626	0.626
$I4_132$	$a = 7.963$	Ni	8*a*	0.125	0.125	0.125
($NiMo_3N$)	$b = 7.963$	Mo	24*h*	0.625	0.140	0.101
	$c = 7.963$	N	8*b*	0.875	0.875	0.875

As shown in Fig. 2, the crystal structures of $P2_13$-$NiMo_4N$ and $I4_132$-$NiMo_3N$ are presented. Table 1 presents the optimized lattice parameters. In the $NiMo_4N$ structure, the N atoms occupy the 4a positions and are coordinated by six surrounding Mo atoms, forming MoN octahedra with a bond length of 2.1 Å. These octahedra are interconnected through corner-sharing. The Ni atoms are located in the voids of the Mo_6N polyhedra, forming an interpenetrating network lattice composed of Mo_6N octahedra and Ni atoms. In the $NiMo_3N$ structure, each N atom is coordinated by six Mo atoms along the axial directions, with bond angles to neighbor-

ing Mo atoms ranging approximately from 87° to 91°. Each Ni atom is connected to three neighboring Mo atoms with a bond length of 2.64 Å, forming equilateral triangles with bond angles of 120°.

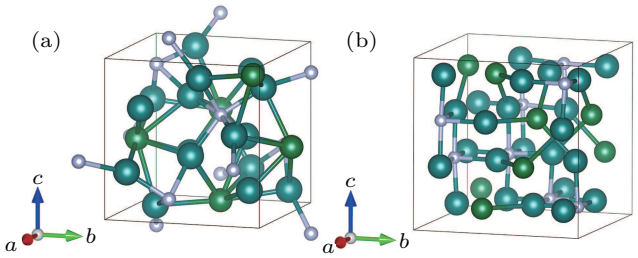


Fig. 2. Crystal structures of Ni_xMo_yN: (a) $P2_13$ phase of $NiMo_4N$ and (b) $I4_132$ phase of $NiMo_3N$.

The electronic properties of $NiMo_4N$ and $NiMo_3N$ were evaluated by calculating their band structures and density of states. Figure 3 shows the band structures and projected density of states (PDOS) of $NiMo_4N$ and $NiMo_3N$. In both structures, bands cross the Fermi level, indicating metallic behavior. The PDOS indicates that Mo-4d orbitals dominate the contribution at the Fermi level. Compared with $NiMo_4N$, the band structure of $NiMo_3N$ is denser, reflecting a more complex electronic structure. The PDOS further shows that in the low-energy region (around −2 eV), Ni-3d orbitals are the main contributors, whereas the conduction bands are primarily derived from Mo-4d orbitals.

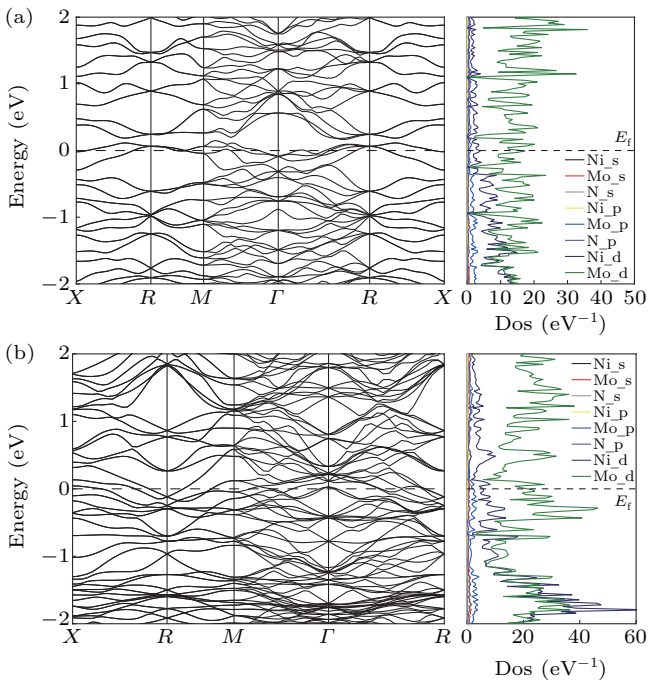


Fig. 3. Electronic band structures (left panel) and partial density of states (right panel) of Ni_xMo_yN: (a) $P2_13$ phase of $NiMo_4N$ and (b) $I4_132$ phase of $NiMo_3N$.

Figure 4 shows the differential charge density of $NiMo_4N$ and $NiMo_3N$, where yellow represents charge accumulation and blue represents charge depletion. The differential charge density indicates electron transfer from Mo atoms to N atoms. Table 2 presents the results of Bader charge analysis, which quantifies this charge transfer in both $NiMo_4N$ and $NiMo_3N$. In the Device Studio software, the valence electron numbers of Ni, Mo, and N were set to 10, 14, and 5, respectively. In the $NiMo_4N$ unit cell, Mo atoms lose a total of 7.85 electrons, while N atoms gain 5.93 electrons. In $NiMo_3N$, Mo atoms transfer 15.53 electrons, while N atoms acquire 12.00 electrons.

Table 2. Bader charge analysis of $NiMo_4N$ and $NiMo_3N$ structures.

	Ni1	Mo1	Mo2	Mo3	Mo4	N1
$NiMo_4N$	10.49	13.40	13.83	13.40	13.83	6.48
$NiMo_3N$	10.44	13.34	13.35	13.36		6.50

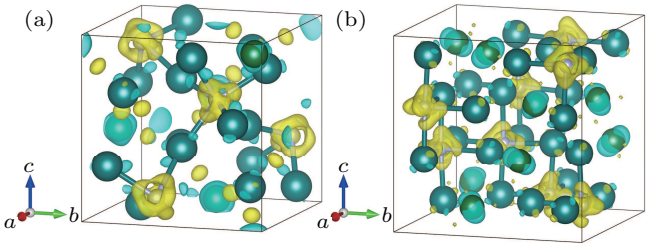


Fig. 4. Differential charge density of $NiMo_xMo_yN$: (a) $P2_13$ phase of $NiMo_4N$ and (b) $I4_132$ phase of $NiMo_3N$.

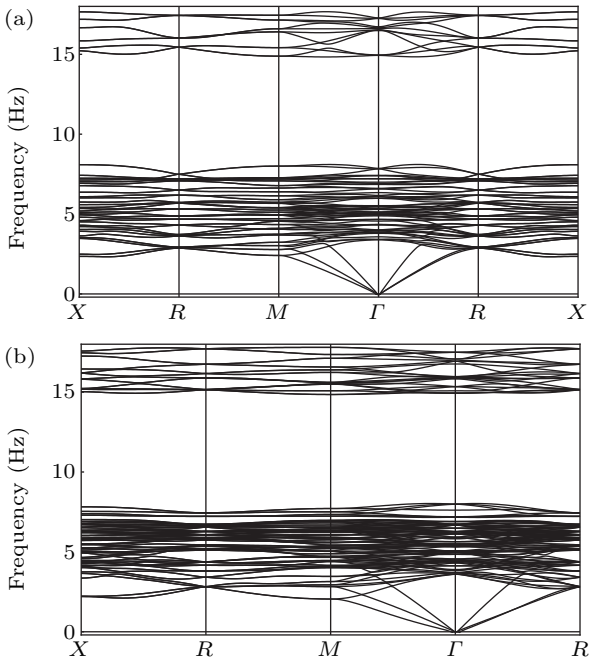


Fig. 5. Phonon dispersion curves of $NiMo_xMo_yN$: (a) $P2_13$ phase of $NiMo_4N$ and (b) $I4_132$ phase of $NiMo_3N$.

To verify the stability of $NiMo_4N$ and $NiMo_3N$, their phonon spectra and elastic constants were calculated. The phonon spectra were obtained using the finite displacement method to assess the dynamical stability of the crystals. Figure 5 presents the phonon spectra of $NiMo_4N$ and $NiMo_3N$, showing no imaginary frequencies throughout the Brillouin zone, which confirms that both structures are dynamically stable.

Table 3. Elastic constants, bulk modulus B (GPa), shear modulus G (GPa), Young's modulus E (GPa), Poisson's ratio ν, and Vickers hardness (GPa) of $NiMo_4N$ and $NiMo_3N$ at 0 GPa.

	C_{11}	C_{44}	C_{12}	B (GPa)	G (GPa)	E (GPa)	ν	H_v (GPa)
$NiMo_4N$	232.49	232.49	84.60	133.90	99.12	238.5	0.20	17.7
$NiMo_3N$	326.45	121.01	227.53	260.50	84.53	228.84	0.35	5.36
Ni_2Mo_3N[33]	471.45	181.60	240.42	317.43	151.47	392.06	0.29	20.5
Pd_2Mo_3N[33]	442.36	141.41	229.73	300.60	126.14	331.99	0.32	17.1
Ni_2Mo_4N[31]	319	98	203	237				

To assess the mechanical stability of $NiMo_4N$ and $NiMo_3N$, they must satisfy the following mechanical stability criteria:[61]

$$C_{11} > 0,\ \ C_{44} > 0,\ \ C_{11} > |C_{12}|,\ \ C_{11} + 2C_{12} > 0. \tag{3}$$

The elastic constants of $NiMo_4N$ and $NiMo_3N$ were calculated using the stress–strain method, as listed in Table 3. The results show that both structures satisfy the criteria for mechanical stability. In addition, the B/G ratios were evaluated, indicating that $P2_13$-$NiMo_4N$ has a B/G of 1.35, below 1.75, corresponding to brittleness, whereas $I4_132$-$NiMo_3N$ has a B/G of 3.08, above 1.75, indicating ductility. The elastic modulus of $NiMo_4N$ is similar to that of Ni_2Mo_4N. The Vickers hardness of both materials was further estimated using the following formula:[62]

$$H_v\ (\text{GPa}) = 2(K^2G)^{0.585} - 3, \tag{4}$$

where $K = G/B$ is Pugh's modulus ratio.

The calculated values are listed in Table 3, showing that the Vickers hardness of $NiMo_4N$ and $NiMo_3N$ are 17.7 GPa and 5.36 GPa, respectively. The hardness of $NiMo_4N$ is comparable to that of Pd_2Mo_3N, while slightly lower than that of the experimentally determined Ni_2Mo_3N structure.

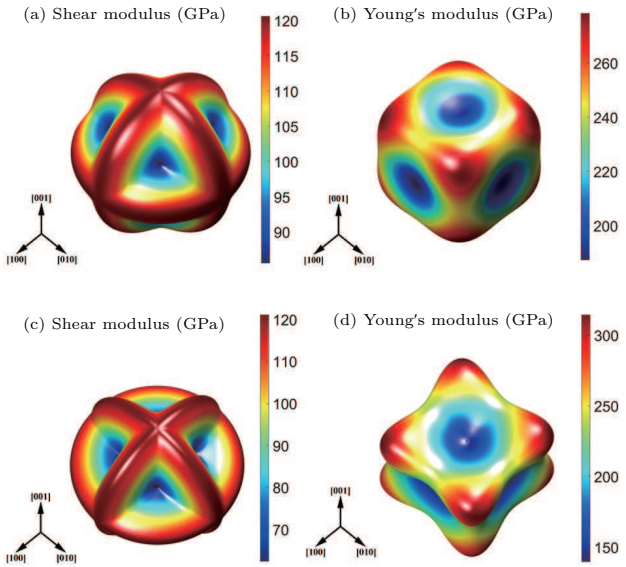


Fig. 6. Three-dimensional representations of (a) shear modulus and (b) Young's modulus of $NiMo_4N$, and (c) shear modulus and (d) Young's modulus of $NiMo_3N$.

Figure 6 also presents the three-dimensional modulus distributions of $NiMo_4N$ and $NiMo_3N$. The results show that the maximum shear modulus for both materials occurs along the principal axes, reaching 121 GPa. Correspondingly, the directions of maximum shear modulus coincide with the minimum Young's modulus, reflecting the anisotropic behavior of these materials. Therefore, the anisotropy indices A^{u} of $NiMo_4N$ and $NiMo_3N$ were calculated, with values of 0.34 and 1.21, respectively. $NiMo_3N$ exhibits stronger anisotropic behavior.[63] The maximum Young's moduli of $NiMo_4N$ and $NiMo_3N$ are 278 GPa and 314 GPa, respectively, indicating that both materials exhibit high stiffness along specific directions. In addition, the bulk moduli of $NiMo_4N$ and $NiMo_3N$ are isotropic in all directions, with values of 133.9 GPa and 260.5 GPa, respectively.

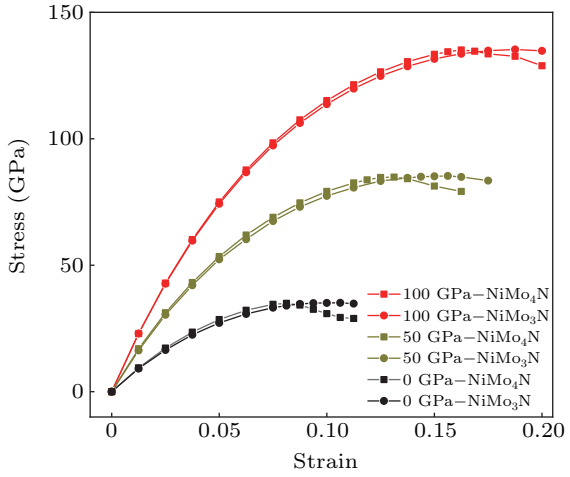


Fig. 7. Tensile stress–strain curves of $NiMo_4N$ and $NiMo_3N$ under different pressures.

To further investigate the deformation behavior of the structures, the ideal tensile strength of the two structures along the [111] crystallographic direction was calculated under different pressures, as shown in Fig. 7. The [111] direction represents a high-symmetry direction in cubic crystal structures, which effectively reflects the material's mechanical limits. The calculation results show that at ambient pressure, the ideal tensile strengths of $NiMo_4N$ and $NiMo_3N$ along the [111] direction are 34.9 GPa and 35.1 GPa, respectively. Their maximum ideal strengths are very close, but their instability behaviors differ significantly. $NiMo_4N$ reaches its peak and becomes unstable at a strain of 0.08, whereas $NiMo_3N$ maintains a relatively high stress level even at a strain of 0.1, demonstrating greater ductility. This result is consistent with

the B/G ratios derived from the elastic constants, further confirming the high-strength brittle nature of $NiMo_4N$. In addition, with increasing pressure, the tensile strengths of both materials increase. At 0 GPa, 50 GPa, and 100 GPa, the ideal tensile strength of $NiMo_4N$ increases from 34.9 GPa $\rightarrow$ 84.9 GPa $\rightarrow$ 134.6 GPa, while the ideal tensile strength of $NiMo_3N$ increases from 35.1 GPa $\rightarrow$ 85.3 GPa $\rightarrow$ 135.1 GPa. The tensile performance of both structures follows a synchronized increase under high pressure, with the ideal tensile strengths remaining close and no sudden change observed under increased pressure.

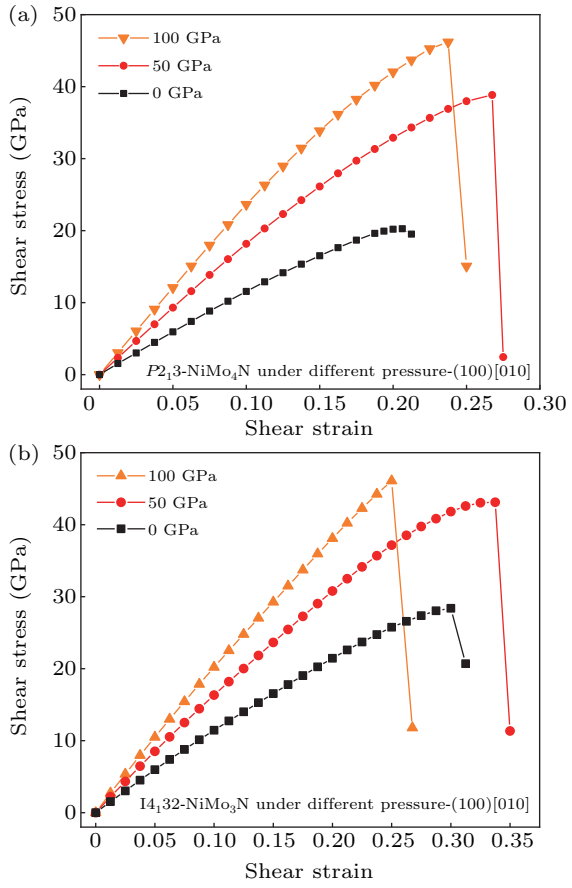


Fig. 8. Shear stress–strain curves under different pressures for (a) $NiMo_4N$ and (b) $NiMo_3N$.

Furthermore, the ideal shear strengths of both structures along the (100)[010] directions under high pressure were also calculated, as shown in Fig. 8. According to the three-dimensional modulus distributions, both materials exhibit the largest shear moduli along the principal axes. Therefore, the (100)[010] directions correspond to the largest ideal shear strengths for both materials. The results show that under high pressure, the ideal shear strengths of $NiMo_4N$ and $NiMo_3N$ increase significantly. For example, at 0 GPa, 50 GPa, and 100 GPa, the shear strength of $NiMo_4N$ increases from 20.3 GPa $\rightarrow$ 38.8 GPa $\rightarrow$ 46.2 GPa, demonstrating excellent shear resistance under high pressure. The increase in shear strength reflects a significant enhancement of the metal–nitrogen bond strength due to the applied pressure, allowing the materials to maintain higher stability under shear stress. Both the ideal shear and tensile strengths increase with pressure, suggesting a positive correlation between lattice compactness and mechanical resistance.

4. Conclusion

Based on CALYPSO structure prediction and first-principles calculations, the $P2_13$-$NiMo_4N$ and $I4_132$-$NiMo_3N$ structures were predicted at ambient pressure. The elastic constants and phonon dispersion curves of both structures confirm their mechanical and dynamical stability. Analysis of the band structures shows that both compounds exhibit metallic behavior, with the Mo-4d orbitals dominating the contributions at the Fermi level, as indicated by the PDOS. The Vickers hardnesses of $P2_13$-$NiMo_4N$ and $I4_132$-$NiMo_3N$ were calculated to be 17.7 GPa and 5.36 GPa, respectively. These hardness values, together with the B/G ratios, indicate that $P2_13$-$NiMo_4N$ behaves as a high-strength brittle material, whereas $I4_132$-$NiMo_3N$ exhibits ductile behavior. Furthermore, ideal tensile strength calculations along the [111] direction show that both materials have similar ideal strengths of approximately 35 GPa at ambient pressure, but their mechanical instability behaviors differ significantly: $P2_13$-$NiMo_4N$ becomes unstable at a relatively small strain, reflecting low ductility, whereas $I4_132$-$NiMo_3N$ maintains high stress at larger strains, demonstrating superior plasticity. These findings are consistent with analyses of elastic moduli and hardness, further confirming the intrinsic relationship between microstructure and mechanical properties. Additionally, under high-pressure conditions, both the ideal shear and tensile strengths increase significantly, indicating that the materials' resistance to tensile and shear stresses is notably enhanced under high pressure.

Acknowledgments

This work was supported by the National Natural Science Foundation of China (Grant No. 11964026), the Natural Science Foundation of Inner Mongolia Autonomous Region of China (Grant Nos. 2019MS01010 and 2023LHMS01014), the Higher Educational Scientific Research Projects of Inner Mongolia Autonomous Region of China (Grant Nos. NJZZ19145 and NJZZ22470), the Doctoral Starting-up Foundation of Inner Mongolia Minzu University of Science and Technology (Grant No. BSZ023), the Inner Mongolia Autonomous Region Youth Capacity Improvement Project (Grant No. GXKY22157), the Higher Physics Major Teaching Steering Committee of the Ministry of Education Project (Grant No. JZW-23-GT-21), and the Scientific Research Fund of Inner Mongolia Autonomous Region of China (Grant No. GXKY25Z050). We gratefully acknowledge HZWTECH for providing computational facilities.

References

[1] Zhang S Y and Zhu W G 1993 *J. Mater. Process. Technol.* **39** 165
[2] Sundgren J E 1985 *Thin Solid Films* **128** 21
[3] Hainsworth S V and Soh W C 2003 *Surf. Coat. Technol.* **163** 515
[4] Polcar T, Martinez R, Vitu T, Kopecky T, Rodriguez R and Cavaleiro A 2009 *Surf. Coat. Technol.* **203** 3254
[5] Navinsek B, Peter P and Ingrid M 1997 *Surf. Coat. Technol.* **97** 182
[6] Qi Z B, Liu B, Wu Z T, Zhu F P, Wang Z C and Wu C H 2013 *Thin Solid Films* **544** 515
[7] Pogrebnjak A D, Beresnev V M, Bondar O V, Postolnyi B O, Zaleski K, Coy E and Araujo J P 2018 *Mater. Des.* **153** 47
[8] Beresnev V M, Bondar O V, Postolnyi B O, Lisovenko M O, Abadias G, Chartier P and Andreev A A 2014 *J. Frict. Wear* **35** 374
[9] Nordin M, Larsson M and Hogmark S 1998 *Surf. Coat. Technol.* **106** 234
[10] Postolnyi B O, Beresnev V M, Abadias G, Bondar O V, Rebouta L, Araujo J P and Pogrebnjak A D 2017 *J. Alloys Compd.* **725** 1188
[11] Tripp W C and Graham H C 1976 *J. Am. Ceram. Soc.* **59** 399
[12] Klemm H, Herrmann M, Reich T and Hermel W 1991 *J. Eur. Ceram. Soc.* **7** 315
[13] Soignard E, Somayazulu M, Dong J, Sankey O F and McMillan P F 2001 *J. Phys.: Condens. Matter* **13** 557
[14] Du P F, Chen L, Zhang X D, Zhang H D, Wang J and Xu Y X 2024 *Ceram. Int.* **50** 47373
[15] Kim N I, Yarali M, Moradnia M, Aqib M, Liao C H, AlQatari F and Ryou J H 2023 *Adv. Funct. Mater.* **332023** 2212538
[16] Xiao S, Suzuki R, Miyake H, Harada S and Ujihara T 2018 *J. Cryst. Growth* **502** 41
[17] Shi Y, Wang X, Zhang L, Chu X, Liu L, Geng B and Zhang H 2025 *Small* **21** 2410803
[18] Ma L, Ting L R L, Molinari V, Giordano C and Yeo B S 2015 *J. Mater. Chem. A* **3** 8361
[19] Cao B, Neuefeind J C, Adzic R R and Khalifah P G 2015 *Inorg. Chem.* **54** 2128
[20] Luo S, Liu Y, Song Y, Yang Y, Chen F, Chen S and Wei Z 2024 *Chem. Commun.* **60** 3295
[21] Zhao J, Zhao Y, Yue W C, Li X, Gao N, Zhang Y J and Hu C Q 2022 *Chem. Eng. J.* **441** 136082
[22] Jing E, Chen L, Xu S, Tian W, Zhang D, Wang N and Qiu X 2022 *J. Energy Chem.* **64** 574
[23] Herle P S, Hegde M S, Sooryanarayana K, GuruRow T N and Subbanna G N 1998 *Inorg. Chem.* **37** 4128
[24] Hund S, Gomez-Capiro O, Ruland H, Heppke E M and Lerch M 2024 *Z. Naturforsch. B* **79** 147
[25] Leybo D V, Arkhipov D I, Firestein K L and Kuznetsov D V 2018 *Catalysts* **8** 436
[26] Leybo D V, Baiguzhina A N, Muratov D S, Arkhipov D I, Kolesnikov E A, Levina V V and Kuznetsov D V 2016 *Int. J. Hydrogen Energy* **41** 3854
[27] Sobhi A S, Bion N, Hargreaves J S, Hector A L, Laassiri S, Levason W and Ritter C 2019 *Mater. Res. Bull.* **118** 110519
[28] Wang L, Xi W, Cheng Q, Zhang K, Liu W, Qin H and Zhou Q 2018 *Chem. Lett.* **47** 20
[29] Tang J, Zhang S, Zeng Y, Yang B, Zhang K, Li Y and Hu J 2024 *Chem. Eng. J.* **487** 150439
[30] Liang C, Li W, Wei Z, Xin Q and Li C 2020 *Ind. Eng. Chem. Res.* **39** 3694
[31] Chen Y, Shen J and Chen N X 2009 *Solid State Commun.* **149** 121
[32] Weil K S, Kumta P N and Grins J 1999 *J. Solid State Chem.* **146** 22
[33] Errandonea D, Ferrer-Roca C, Martinez-Garcia D, Segura A, Gomis O, Munoz A and Sapina F 2010 *Phys. Rev. B* **82** 174105
[34] Zaman S F, Jolaoso L A, Podila S, Al-Zahrani A A, Alhamed Y A, Driss H and Petrov L 2018 *Int. J. Hydrogen Energy* **43** 17252
[35] Bem D S, Gibson C P and Loye H C 1993 *Chem. Mater.* **5** 397
[36] Wang Y, Lv J, Zhu L and Ma Y M 2010 *Phys. Rev. B* **82** 09411
[37] Wang Y, Lv J, Zhu L and Ma Y M 2012 *Comput. Phys. Commun.* **183** 2063
[38] Lu C, Gong W, Li Q and Chen C 2020 *J. Phys. Chem. Lett.* **11** 9165
[39] Zhang L, Wang Y, Lv J and Ma Y M 2017 *Nat. Rev. Mater.* **2** 17013
[40] Wang Y and Ma Y M 2014 *J. Chem. Phys.* **140** 040901
[41] Lu C, Li Q, Ma Y M and Chen C 2017 *Phys. Rev. Lett.* **119** 115503
[42] Li Y, Wang Y, Pickard C J, Needs R J, Wang Y and Ma Y M 2015 *Phys. Rev. Lett.* **114** 125501
[43] Li P F, Du X, Gao G, Sun R, Zhang L and Wang W 2020 *Comp. Mater. Sci.* **171** 109205
[44] Li P F, Mei T T, Lu Z, Xiang L, Zhang X, Du X, Wang J J and Chen H H 2018 *Comp. Mater. Sci.* **159** 428
[45] Chen B, Conway L J, Sun W, Kuang X, Lu C and Hermann A 2021 *Phys. Rev. B* **103** 035131
[46] Li P F, Lang H Y, Bao X, Feng C, Xing S Y, Lin J and Ma X J 2022 *Comp. Mater. Sci.* **207** 111310
[47] Bao X, Lang H Y, Ma X J, Ou T J, Zhang M G, Zhang X and Li P F 2022 *Solid State Commun.* **342** 114635
[48] Liu G, Wang H, Ma Y and Ma Y M 2011 *Solid State Commun.* **151** 1899
[49] Hamlin J 2015 *Phys. C* **514** 59
[50] Eberhar R and Kennedy J 1995 *Proceedings of the Sixth International Symposium on Micro Machine and Human Science*, October 4–6, 1995, Nagoya, Japan, pp. 39
[51] Kennedy J and Eberhart R 1995 *Proceedings of ICNN'95-International Conference on Neural Networks*, November 27–December 01, 1995, Perth, Australia, pp.1942
[52] Wang T, Wen M H, Zhang X X, Wang W H, Liu J M, Wang X Y and Li P F 2025 *Chin. Phys. B* **34** 036104
[53] Perdew J P, Burke K and Ernzerhof M 1996 *Phys. Rev. Lett.* **77** 3865
[54] Perdew J P, Chevary J A, Vosko S H, Jackson K A, Pederson M R, Singh D J, Fiolhais C 1992 *Phys. Rev. B* **46** 6671
[55] Kresse G and Furthmüller J 1996 *Phys. Rev. B* **54** 11169
[56] Perdew J P, Burke K and Ernzerhof M 1996 *Phys. Rev. Lett.* **77** 3865
[57] Blochl P E 1994 *Phys. Rev. B* **50** 17953
[58] Togo A, Oba F and Tanaka I 2008 *Phys. Rev. B* **78** 134106
[59] Wu Y, Lazic P, Hautier G, Persson K and Ceder G 2013 *Energy Environ. Sci.* **6** 157
[60] Hinuma Y, Hatakeyama T, Kumagai Y, Burton L A, Sato H, Muraba Y and Oba F 2016 *Nat. Commun.* **7** 11962
[61] Mouhat F and Coudert F X 2014 *Phys. Rev. B* **90** 224104
[62] Chen X Q, Niu H Y, Li D Z and Li Y Y 2011 *Intermetallic* **19** 1275
[63] Ranganathan S I and Ostoja-Starzewski M 2008 *Phys. Rev. Lett.* **101** 055504